A Finite Difference Forward Model for MEG and EEG

by

Omri Schwarz

Submitted to the Department of Electrical Engineering and Computer Science
in Partial Fulfillment of the Requirements for the Degrees of

Bachelor of Science in Electrical Engineering and Computer Science

and

Master of Engineering in Electrical Engineering and Computer Science

at the

MASSACHUSETTS INSTITUTE OF TECHNOLOGY

August 29, 2003 [September 2006]

Author .....
Department of Electrical Engineering and Computer Science
August 29, 2003

Certified by .....
Eric Grimson
Gordon Professor of Medical Engineering
Thesis Supervisor

Accepted by .....
Arthur C. Smith
Chairman, Department Committee on Graduate Students

A Finite Difference Forward Model for MEG and EEG

by

Omri Schwarz

Submitted to the Department of Electrical Engineering and Computer Science
on August 29, 2003, in Partial Fulfillment of the
Requirements for the Degrees of
Bachelor of Science in Electrical Engineering and Computer Science
and
Master of Engineering in Electrical Engineering and Computer Science

Abstract

In this thesis, I designed and implemented a model of the electromagnetic signals generated by the human brain as seen on magnetoencephalography and electroencephalography machines. The model makes a novel use of the principle of reciprocity combined with Ohm's Law and the Biôt Savart Law to build a model of the human magnetoencephalogram that is much faster to compute than the current state of the art.

The model uses an existing finite difference model for electroencephalography and modifies it to incorporate the Biôt Savart Law into its geometry. I tested the model against a spherical model to show that it is highly sensitive to approximations made of the Biôt Savart Law for finite plane-bounded elements, but that further refinements of the model could make it as accurate as regular finite element models for magnetoencephalography.

Thesis Supervisor: Eric Grimson
Title: Gordon Professor of Medical Engineering

Acknowledgments

For bringing me into the world, putting me through what is politely known as an academic career, and putting up with my existence up until now, I would like to thank my mother, Carol Bourne.

For the financial and logistic support that has made this project possible, I must thank my uncle Samuel Anderson, and his dear friends William Barton Rogers and Robert Oppenheimer. For arranging a different sort of logistic assistance, and smoothing the path to this day for indeed a small price, I thank Mephistopheles.

For the academic supervision and help without which this thesis would not be written, I must thank a cast of hundreds, among which are John S. George of the Los Alamos National Laboratory, David S. Tuch, Jack Belliveau, Eric Grimson, and sundry others.

For showing that all the hardship in the world cannot stop a good idea from finally coming to light, I thank my fellow Chicagoans Wesley Willis and Henry Darger, and also John Nash. For dissuading me from taking a different path, I pay homage to the poetess and patron saint of graduate students, Dorothy Parker. Finally, for putting this project in proper perspective, I thank Christopher Lloyd and Howard Phillips Lovecraft.

Contents

List of Figures

Chapter 1

Introduction

1.1 Origins of the EEG and MEG

The human brain has been an object of curiosity and study since the days of Aristotle. The ability to monitor the activity of a human brain is of great use to clinicians and researchers, and so there are several methods for doing so. Functional magnetic resonance imaging, positron emission tomography, and single photon emission computed tomography allow the monitoring of the metabolic behavior of the brain, with a resolution on the order of tens of seconds. Electroencephalography (EEG) and magnetoencephalography (MEG) enable us to monitor brain activity with a time-resolution on the order of milliseconds. It is believed that the MEG/EEG signal is generated by synchronous postsynaptic potentials in large numbers of neurons, large enough to be summed up to a signal at a large, remote EEG scalp electrode. Besides being synchronized, the neurons need to be aligned enough with each other to amplify each other's extracellular potential fields. The pyramidal cells of the cerebral cortex are arranged so that their dentrites are parallel with each other and perpendicular to the cortical surface, and are thus believed to be the source of the EEG/MEG signal.

The electroencephalogram measures potential differences between scalp electrodes as a function of time. Its popularity derives from the low cost of the hardware it requires, and from its millisecond temporal resolution, which allows the observation of sub-second neural processes. Its chief disadvantage is its poor spatial resolution.

To reach the surface electrodes, potentials generated in the brain must travel through brain, cerebro-spinal fluid, skull and scalp, and are attenuated and spread through the scalp. This blurring effect is mitigated partly by some methods[20] but is still the spur for the development of the magnetoencephalogram.

The magnetoencephalogram measures the magnetic field a short distance from the head, using superconducting quantum interference devices (SQUIDs), and traces it as a function of time, with a similar temporal resolution. It detects deeper brain activity with greater sensitivity, and discriminates more in favor of sources near the sensor, allowing us a better opportunity to locate the source. Its disadvantages are that it is insensitive to sources that are oriented normally to the scalp surface, and requires an expensive and cumbersome apparatus. It is an increasingly used method for observing brain activity because it suffers far less than the EEG from the blurring effect caused by the skull's low conductivity.

Even alone, the waveforms seen on the EEG and MEG can provide a wealth of information. Literature abounds about such waveforms as "the P300" and the "N70." These are waveforms observed empirically on the EEGs of patients and subjects in various situations over the decades in which EEG has been in use. But there is more to be learned and diagnosed by localizing the neurons that generate these waveforms. Localization can bring more insight into the subcomponents of long-known waveforms[11, 23]. The methods used for source localization can benefit from improved accuracy and lowered computational cost, and the reciprocity-based forward model for the MEG, described herein, may well do both.

1.2 The Forward and Inverse Problems

The inverse problem (IP)[7, 25], an important challenge for neuroscience, is the problem of identifying accurately, non-invasively and in real time, which regions of a subject's brain are active, given electroencephalographic (EEG) or magnetoencephalographic data collected outside the scalp. Estimating the location and orientation of electric current sources within the brain from such data is an ill-posed problem. Given

a set of MEG or EEG data, one can find an infinite set of source configurations in the brain that could have produced it. This is what classifies this challenge as an inverse problem, a term of art that applies to such mathematical problems in numerous contexts. A more modest challenge, the forward problem (FP), is that of calculating what an EEG or MEG dataset would look like for a positted configuration of sources. Some attempts to solve the IP begin by calculating a forward solution for a positted source configuration and then adjusting it iteratively until the waveforms shown by the forward solver are close enough to the given EEG/MEG data (e.g. a downhill simplex method in Ranken et al [16]). The accuracy of any such inverse solver is therefore highly dependent on that of the forward solver on which it relies.

The forward problem begins with known distributions of the conductivity σ and the brain's electrical current generators, as is reviewed in Hämäläinen et al.[13] It therefore requires Maxwell's equations and the continuity equation $\vec{\nabla} \cdot \vec{J} = \partial\rho/\partial t$ to calculate $\vec{E}$ and $\vec{B}$, the electric and magnetic fields. $\vec{J}$ and ρ are the total current density and charge density, respectively.

$$\vec{\nabla} \cdot \vec{E} = \frac{\rho}{\epsilon_0}, \tag{1.1}$$

$$\vec{\nabla} \times \vec{E} = -\frac{\partial \vec{B}}{\partial t}, \tag{1.2}$$

$$\vec{\nabla} \cdot \vec{B} = 0, \tag{1.3}$$

$$\vec{\nabla} \times \vec{B} = \mu_0(\vec{J} + \epsilon_0 \partial \vec{E}/\partial t). \tag{1.4}$$

In a passive nonmagnetic medium, $\vec{J}$ is the sum of ohmic volume current and the polarization current, i.e.

$$\vec{J} = \sigma \vec{E} + \partial \vec{P}/\partial t, \tag{1.5}$$

where $\vec{P}$ is the polarization vector.

According to Hämäläinen et al[13], electromagnetic phenomena in the human head are in the frequency range of 1 khz and under. EEG/MEG sources are slow-changing enough, therefore, that the fields they generate depend on the head's conductivity

distribution and not on any complex impedance. Thus, quasistatic assumptions[42] apply in the EEG/MEG forward problem. The forward problem consists of solving the Poisson equation for the electrostatic potential given the configuration of brain activity sources and our model for the subject's head. The electrostatic potential ϕ below is determined by the conductivity as per the left hand side and by the sources, which may be current sources (right hand side) or points where the potential is clamped to some value. The conductivity $\overline{\overline{\sigma}}$ may take a scalar value or it may be a 3-by-3 symmetric tensor, in fibrous tissue regions where current flows more readily in the direction of nerve or muscle fibers than across them.

$$\vec{\nabla}\overline{\overline{\sigma}}\vec{\nabla}\phi = \vec{\nabla}\cdot\vec{j} \tag{1.6}$$

It is useful to describe the electric currents through the head, $j(\vec{r})$, as the sum of a primary current $j^p(\vec{r})$ generated by brain activity and a return current, $j^v(\vec{r}) = \sigma\vec{\nabla}V(\vec{r})$, brought about by the conductivity of the medium. Once the forward problem is solved for the electrostatic potential $V(\vec{r})$, and therefore $j(\vec{r})$, one can obtain the magnetic field $B(\vec{r'})$ outside the head. In the quasistatic case, the Biôt Savart Law applies.

$$\vec{B}(\vec{r'}) = \frac{\mu_0}{4\pi}\iiint \frac{\vec{j}(\vec{r})\times\hat{R}}{R^2}dv \tag{1.7}$$

Here $\vec{r'}$ is the point where the field is observed, and $\vec{R} = \vec{r'} - \vec{r}$. Separating the primary and return currents yields separate definitions for the magnetic fields induced by each. B_0 is the field induced by the primary current and B_v is that induced by the return current.

$$\vec{B_0}(\vec{r'}) = \frac{\mu_0}{4\pi}\iiint \frac{\vec{j^p}(\vec{r})\times\hat{R}}{R^2}dv \tag{1.8}$$

$$\vec{B_v}(\vec{r'}) = -\frac{\mu_0}{4\pi}\iiint \frac{\sigma\vec{\nabla}\phi\times\hat{R}}{R^2}dv \tag{1.9}$$

Fast solvers exist that use a spherical head model [5, 32, 45, 4]. Others use standardized realistic head models and finite element or boundary element methods. One can also use realistic head models that are built of each subject's anatomy thanks

to segmented nuclear magnetic resonance imaging scans. In these anatomical scans manual or automatic algorithms are used to assign conductivity values to each element by tissue type. The electrostatic conductivity can also be measured in vivo by diffusion-weighted magnetic resonance imaging. In the realistic forward models, we solve for the potential by solving for Poisson's equation constrained by the Von Neumann boundary condition (that there is no current going from the subject to the surrounding air), and by the source configuration (which can be depicted as a current source or as a second boundary in which the Dirichlet condition applies, i.e. the potential is given a priori). Whether given as current sources or as Dirichlet boundaries, source configurations are usually shaped as simple dipoles, since early literature argued that dipoles are an adequate model for brain activity[6]. Since then some work has shown that a distributed source model[17] can give more consistent localizations for discrete events like the N70 waveform[35]. Any distributed current source, however, can easily be represented by a sum of current dipoles.

Realistic head models also depend on the values given for the electric conductivity of each compartment in the brain. Models commonly assign to each segmented compartment a value from the literature. In vivo the conductivity is not uniform in each type of tissue. In fact, for some tissues (white and gray matter, muscle, soft bone), the conductivity is anisotropic, that is, the tissue conducts electricity better in some directions than in others. However, a method exists for measuring the anisotropic conductivity distribution in vivo, using diffusion-weighted magnetic resonance imaging[18, 34]. In the anisotropic case, a forward model can treat the electric conductivity as a 3 by 3 symmetric tensor value rather than a scalar. A finite difference model exists for handling anisotropic conductivity in box-shaped compartments[28, 29].

The accuracy of a forward model can first be validated by seeing how closely it can comply with analytical solutions to Poisson's equation. In [28], the model is run for a cubic volume and a Dirichlet boundary condition matching a potential distribution in an infinite homogenous medium. The calculated potential inside the cube was close enough to satisfy Saleheen and Ng[28, 29]. Another step one can take is to calculate

the potential distribution for a discretized multilayered sphere and compare it to a semi-analytical solution (several exist[30, 4, 5, 32, 46, 45]). Schimpf et al have shown that there are systemic errors in such comparisons[31].

The validation of an inverse model begins with positting a head model and source, generating a forward solution, adding random noise, and running the inverse model to see if it gives an accurate guess as to the source. Its usability depends on what signal to noise ratio the inverse model requires to give an accurate answer, and also how it can handle more systemic errors such as an inaccurate head model or one misaligned with the sensors involved. Better validation comes by combining EEG/MEG with simultaneous observation of brain activity by another modality, such as functional MRI[22, 33].

1.3 The MEG Forward Problem

The simplest forward model for the MEG is that of a dipole source in a multilayered sphere. The symmetry of the sphere dictates that dipole sources that are radially oriented will generate no magnetic field at all outside the sphere[30], and indeed, the MEG of human brain activity is insensitive to sources that are normally oriented to the scalp. The model also dictates high sensitivity to sources that are oriented parallel to the surface, as again is seen in the MEG. A forward solver does exist that uses Sarvas's spherical model by fitting a sphere to the shape of the subject's head[24]. Neither rule holds absolutely in vivo, however. The asymmetry and anisotropy of the human head call for the use of better forward models for the MEG.

The boundary element method incorporates information about the shape of the skull to form a forward model for the MEG[8]. It remains the commonly used forward model for MEG, because of its speed and modest demands for computer memory. It, however, divides the head into compartments of uniform, isotropic conductivity, and is thus itself unsatisfactory. It cannot account for anisotropic conductivity, nor for the apertures of the optic and auditory nerves. Finite element methods (e.g. [40]) can incorporate all information available about the head geometry, including anisotropic

conductivity, which is believed to be important enough that including it will improve the performance of a forward solver (and the inverse solvers that depend on it)[15, 14]. Their disadvantage comes from the high demands they place on computer memory and computer time. The finite element method is limited in the fidelity with which it can represent dipolar current sources in the head, and the iterative matrix inversion methods on which it relies are all slow to converge when they solve for the potential generated by a concentrated source configuration such as a dipole. Also, the inverse problem consists of finding a source of an EEG signal from millions of possible source configurations. To do so in reasonable time requires a shortcut. For the EEG inverse problem, two shortcuts exist.

Instead of solving the forward problem for each possible dipole, one can decimate the set of dipoles by some factor, solve for each dipole of this set, that is spread throughout the volume, and for dipoles that are not in the set, use an interpolation of nearby dipoles that were calculated. This method is in use for MEG[44]. A more interesting method is to use the principle of reciprocity as described in the next chapter to calculate the forward problem not for each dipole but for each sensor. The advantage of repeating the process for up to 256 electrodes rather than 1,000,000 dipoles is quite obvious. What is not so obvious, but which this thesis explores, is the use of reciprocity to solve the forward problem in MEG, also, for every sensor rather than every source.

Chapter 2

The Reciprocity Theorem

2.1 Reciprocity derived for EEG

The reciprocity theorem is a useful way to get around complicated problems in homework assignments in electricity and magnetism classes. It's also a useful tool for forward modeling for electroencephalography. We begin by looking at Plonsey's derivation of it for EEG[26].

We take two scalar functions ϕ and ψ that are subject to Poisson's equation, on the same volume. Using standard vector identities we can construct

$$\vec{\nabla} \cdot \phi(\sigma\vec{\nabla}\psi) = \phi\vec{\nabla} \cdot (\sigma\vec{\nabla}\psi) + \sigma\vec{\nabla}\psi \cdot \vec{\nabla}\phi \tag{2.1}$$

and

$$\vec{\nabla} \cdot \psi(\sigma\vec{\nabla}\phi) = \psi\vec{\nabla} \cdot (\sigma\vec{\nabla}\phi) + \sigma\vec{\nabla}\phi \cdot \vec{\nabla}\psi. \tag{2.2}$$

Subtracting 2.2 from 2.1, using the commutative property of the dot product, and integrating over the volume, we get:

$$\int_V \vec{\nabla} \cdot \phi(\sigma\vec{\nabla}\psi)dV - \int_V \vec{\nabla} \cdot \psi(\sigma\vec{\nabla}\phi)dV = \int_V \phi\vec{\nabla} \cdot (\sigma\vec{\nabla}\psi)dV - \int_V \psi\vec{\nabla} \cdot (\sigma\vec{\nabla}\phi)dV \tag{2.3}$$

The divergence theorem can turn the volume integrals on the left hand side into

surface integrals:

$$\int_s \phi(\sigma\vec{\nabla}\psi)\cdot \mathrm{d}\vec{S} - \int_s \psi(\sigma\vec{\nabla}\phi)\cdot \mathrm{d}\vec{S} = \int_V \phi\vec{\nabla}\cdot(\sigma\vec{\nabla}\psi)dV - \int_V \psi\vec{\nabla}\cdot(\sigma\vec{\nabla}\phi)dV \quad (2.4)$$

In Plonsey's application to the electrocardiographic problem, he lets ϕ be the scalar potential arising from an arbitrary volume source $\vec{J}_i$. Since the total current, $\vec{J}_i - \sigma\vec{\nabla}\phi$ is solenoidal with zero divergence, ϕ is subject to the familiar equation

$$\vec{\nabla}\cdot(\sigma\vec{\nabla}\phi) = \vec{\nabla}\cdot\vec{J}_i \quad (2.5)$$

and also to the Von Neumann boundary condition forced by the non-conductivity of the surrounding air.

$$\sigma\vec{\nabla}\phi\cdot\vec{n} = 0 \quad (2.6)$$

Now we define ψ in order to employ reciprocity. A unit of current is inserted in one point in the body, a, and removed in an adjacent point, b, inducing a scalar electric potential throughout the body. In the case of EEG, the two points would be on the surface, where a reference and measurement electrode are placed, and therefore would require this:

$$\sigma\vec{\nabla}\psi\cdot\vec{n} = \delta_s(\vec{r}-\vec{a}) - \delta_s(\vec{r}-\vec{b}) \quad (2.7)$$

Here, δ_s is the two dimensional Dirac delta function, $\vec{r}$ is the independent position vector, and $\vec{a}$ and $\vec{b}$ are the position vectors of the two points. And, here we depart from Plonsey and instead require that the two points be within the volume. We use the three dimensional Dirac function δ_v and that means ψ obeys the following conditions:

$$\sigma\vec{\nabla}\psi \cdot \vec{n} = 0 \tag{2.8}$$

$$\vec{\nabla} \cdot (\sigma\vec{\nabla}\psi) = \delta_v(\vec{r} - \vec{a}) - \delta_v(\vec{r} - \vec{b}) \tag{2.9}$$

Substituting 2.5-2.7 into 2.4 gives the following result, which as you will note, does not depend on the function σ within V:

$$\phi(a) - \phi(b) = \int_V \psi\vec{\nabla} \cdot \vec{J}_i dV. \tag{2.10}$$

Now suppose that the electroencephalographic source that has drawn our interest can be described as a "physical dipole," i.e. a point current source at $\vec{r_1}$ and sink at $\vec{r_2}$. Again the three-dimensional Dirac delta function comes in:

$$\vec{\nabla} \cdot \vec{J}_i = \delta_v(\vec{r} - \vec{r_1}) - \delta_v(\vec{r} - \vec{r_2}) \tag{2.11}$$

Plugging 2.11 into 2.10 we get

$$\phi(a) - \phi(b) = \psi(r_1) - \psi(r_2). \tag{2.12}$$

The use of the reciprocity theorem for the EEG forward problem is described in [3, 26, 19, 9, 10, 47, 41, 43] and demonstrated below. The forward model is calculated for a source distribution with a current source at the sensor electrode and an equal sink at the ground electrode. The potential difference between the electrodes for any dipole in the volume is then calculated thus:

$$\Delta\phi = \frac{\vec{E} \cdot \vec{p}}{I}. \tag{2.13}$$

$\Delta\phi$ is the potential difference between the electrodes, $\vec{E}$ is the electric field at the location of the dipole, (and is simply the local potential gradient), I is the current at the source and sink, and $\vec{p}$ is the dipole moment. In figure 2.1, the forward model used in this thesis was run on a segmented MRI volume, with the sources on the

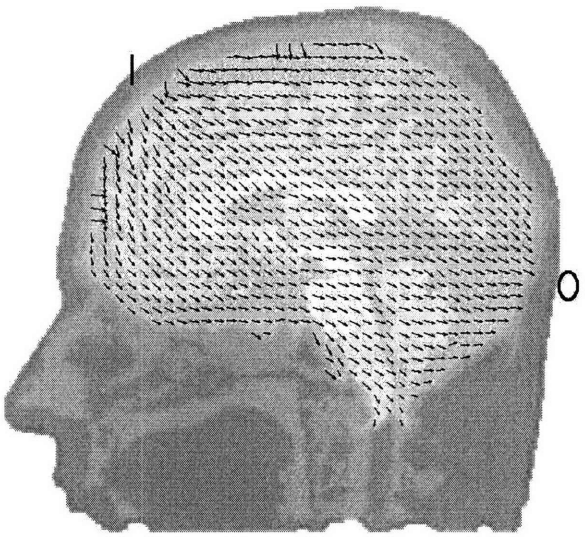

Figure 2-1: An example of an EEG reciprocity solution

midsaggital plane marked as I and O. The arrows show the electric field in the area within the skull (the magnitude is distorted to emphasize the direction of the field). Having calculated the potential distribution for each electrode, we are left free to search for source distributions that fit our data. Each distribution can be tested with little more than a memory lookup and a few multiplications per source.

The volume conduction effect of the skull proves a nuisance in this context. In figure 2.1 are pseudocolor plots of the magnitude of the electric field for this context, with the same source locations and slice selected, but in the second the skull segmentation has been replaced with voxels of conductivity of $0.33Sm^{-1}$. Any iterative inverse solver will lean toward solutions in areas of a high field magnitude. The presence of the skull pushes the solvers to areas just within the skull boundary.

2.2 Reciprocity applied to MEG

The reciprocity rule is already being applied for EEG. For MEG, however, the rule is not so simple to apply. An analytical spherical model has been written for the mag-

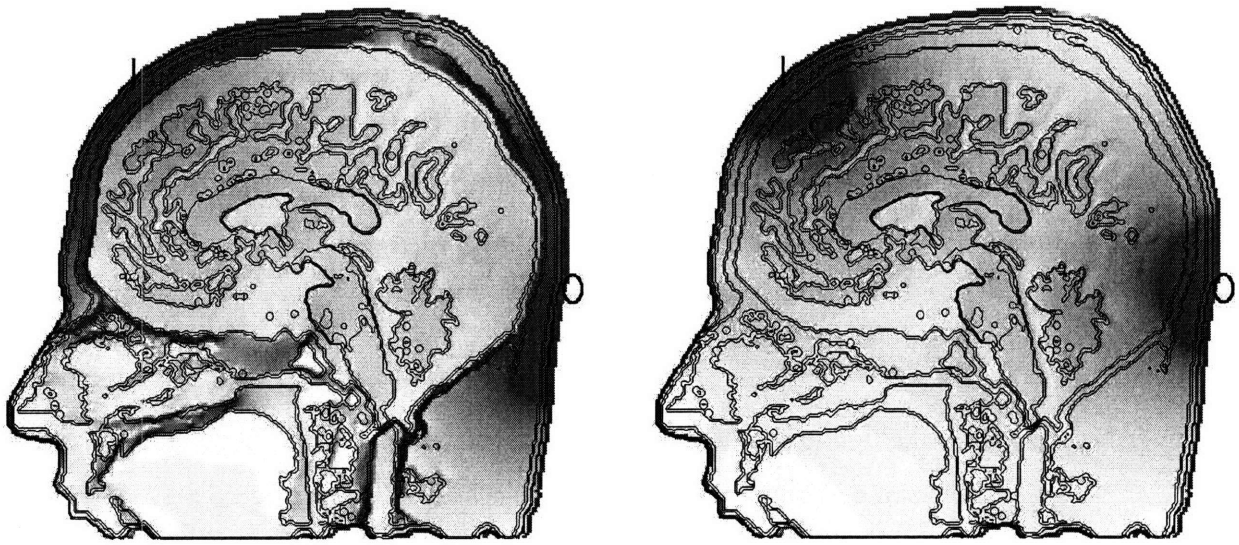

Figure 2-2: Inverse solvers need a search space with a well defined optimum solution to avoid searching through local minimaoptima and spaces with a weak gradient. Above is a pseudo-color plot of a regular reciprocity solution (left) with the two sources marked, and on the right a one with the skull replaced with scalp tissue. The color encodes local electric field magnitude.

netic field outside a volume conductor [30], and is in use by several research groups. In Van Uitert et al[38] and followup work[36], it was shown that the spherical model is of limited use in estimating magnetic fields generated by inhomogenous conductors. Boundary element solvers also exist. Finite element solvers also exist: these calculate the potential distribution due to a dipole and then calculate the magnetic field using the Biôt-Savart Law. To do so for each dipole is too time consuming for any iterative inverse solver. One approach to this problem is to perform the forward solution for a set of proposed dipole locations, and then interpolate between these for any other proposed location[44].

Now we set out to apply equation 2.12 to the MEG forward problem. We assume that our case is quasistatic, and so the way to calculate the magnetic field at a sensor point r_s outside the volume is to calculate the potential throughout V as induced by the dipole in $a - b$ and then integrate the Biôt-Savart equation as in equation 2.14. This we must do both for the current dipole and for the currents it forces throughout

the volume [39, 38, 37].

$$\vec{B} = \frac{\mu_0}{4\pi} \iiint_V \frac{\vec{j} \times \hat{r}}{r^2} dv. \tag{2.14}$$

A common way to calculate Biôt-Savart in finite element or finite difference schemes is to calculate the current through each face, and calculate Biôt-Savart for a line segment going from the element's centroid to that face. In that case the equation simplifies:

$$\vec{B} = \frac{\mu_0}{4\pi} \int \frac{\vec{I} \times \hat{r}}{r^2} dl. \tag{2.15}$$

For a straight line segment, 2.15 integrates to a function of distances from the sensor to the two endpoints (r) and the distances along the axis formed by the segment (l):

$$B = \frac{\mu_0 I}{4\pi R} \left(\frac{l'}{r'} - \frac{l}{r} \right) \tag{2.16}$$

Each element has three current components I_x, I_y, and I_z, that are determined by the gradient of the electrostatic potential. The magnetic field at our point of observation, also has the three components B_x, B_y, and B_z. By Biôt-Savart, B_x depends only on I_y, and I_z. Each I_y is determined by a $\Delta_y \phi$, a difference in the potential between two adjacent points in the volume. Those two points now become the r_1 and r_2 in 2.10. To go from $\Delta_y \phi$ to I_y and finally to B_x requires a set of summations.

$$B_x = \sum W_{xy} \Delta_y \phi + \sum W_{xz} \Delta_z \phi \tag{2.17}$$

W_{xy} and W_{xz} are coefficients assigned by the discretized Biôt Savart equation and the Ohm's Law relation between potential and current. They carry units of Tesla per Volt. The summation is done for all adjacent elements in the y and z directions. But now, instead of calculating ϕ for a dipole source and then going through the Biôt-Savart step, we can assign a source configuration weighted by the W functions, run the forward modeler, and then refer to the principle of reciprocity. The particulars of

the W functions are discussed in the next section.

In the EEG context, the equation being solved is Poisson's equation, either for a dipole configuration or for a source configuration governed by reciprocity:

$$\vec{\nabla}\bar{\bar{\sigma}}\vec{\nabla}\phi = \vec{\nabla}\cdot\vec{j} \tag{2.18}$$

The operator $\vec{\nabla}\bar{\bar{\sigma}}\vec{\nabla}$ is discretized to a finite element mesh (hexahedral in this case) and represented by a sparse matrix A that is then inverted by whatever method to solve for ϕ sampled in the mesh nodes (and called x), with a known distribution of current sources represented by the discretized form of $\vec{\nabla}\cdot\vec{j}$ (called b). To apply reciprocity we set b at each node to be the sum of all positive and negative values of W_{xy} and W_{xz} that apply to it. In differential form, equation 2.18 combines with equation 1.9, constrained to one directional component of the magnetic field, (noted as $\hat{B}$) to form a new relation at each point throughout the volume:

$$\vec{\nabla}\bar{\bar{\sigma}}\vec{\nabla}\phi = \frac{\mu_0\bar{\bar{\sigma}}\vec{\nabla}\psi\times\hat{R}\cdot\hat{B}}{4\pi R^2}. \tag{2.19}$$

It is worth noting that in a infinite homogenous space equation 2.19 simplifies to

$$\nabla^2\phi = \frac{\mu_0\vec{\nabla}\psi\times\hat{R}\cdot\hat{B}}{4\pi R^2}. \tag{2.20}$$

In a finite element scheme, the conductivity distribution is discretized by selecting a set of points to form the nodes, selecting a set of functions called basis functions that describe the relationship of the nodes to the space surrounding them. In a linear finite element scheme, the basis functions are scalars with a value of 1 at the node point itself and decline linearly to 0 from the node to its nearer neighbors. ψ above is the basis function for a node in a finite difference scheme (a finite difference scheme is a subset of finite element, in which the nodes are arranged in a regular Cartesian grid). Multiply the right hand sign of equation 2.19 by the basis function for each node and integrate for the volume, and you will have the W coeeficients needed for a reciprocity-based lead field for a magnetoencephalography forward solution.

2.3 The Biôt-Savart Law

The Biôt-Savart Law does not integrate gracefully for linear current density distributions in plane-bounded elements. When integrated over an plane-bounded element, the Biôt-Savart Law has a singularity at each corner. Nevertheless, there are some papers on this issue, recapped here[2]. A first approximation to calculating the integral over a finite element is to have line segments from the centroid to each face represent the current out of that face and then calculate the integral for each of these line segments. The accuracy of that approximation depends on the distance from the element to the sensor point as compared to the characteristic dimension of the element. The simplest approximation for a hexahedral element is of a current line segment running from the center of one face to that of the opposite. If the element is distant from the sensor, it generates a field magnitude B from its current (presumed to be in the y direction) as shown below:

$$B = \frac{\mu_0 I}{4\pi R} \frac{l_y}{r} \tag{2.21}$$

R is the distance from the sensor to the axis formed by line segment, l is the position on that axis of the two points forming the segment, r is the distance from the sensor to each of the points, and B is the magnetic field strength. Let l_x, l_y, l_z be the inter-voxel spacings on each axis. These conventions hold throughout this section. For a line segment that is nearer the sensor, the magnetic field looks thus:

$$B = \frac{\mu_0 I}{4\pi R}(\frac{l'}{r'} - \frac{l}{r}) \tag{2.22}$$

Since $l' - l$ is the inter-element resolution, to calculate B_x as induced by an I_y current component, we fill in what l is and add one factor: B has x and z components, and we need just one of them, so we multiply by $\frac{z}{\sqrt{x^2+z^2}}$. (For simplicity, we put the sensor at the Cartesian origin.)

$$B_x = \frac{\mu_0 I z}{4\pi(x^2+z^2)}(\frac{y+l_y}{\sqrt{x^2+(y+l_y)^2+z^2}} - \frac{y}{\sqrt{x^2+y^2+z^2}}) \tag{2.23}$$

For observations distant from the line segment, $l_y << x, z$, and putting the Cartesian coordinates into Equation2.21 yields this:

$$B_x = \frac{\mu_0 I z l_y}{4\pi(x^2+z^2)\sqrt{x^2+y^2+z^2}} \tag{2.24}$$

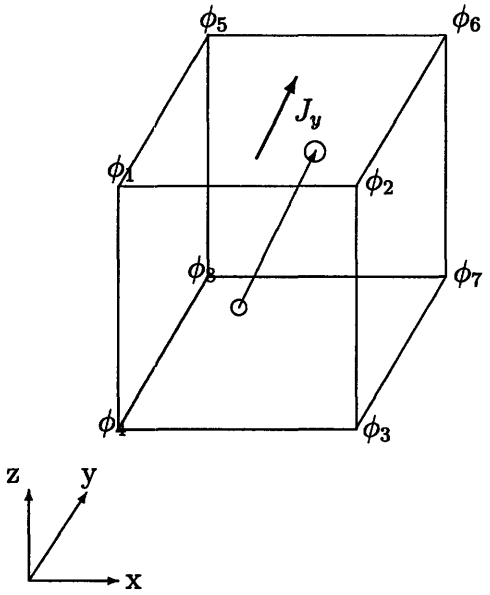

Figure 2-3: How a voxel appears in the Biôt-Savart equation

Figure 2.3 shows the important details of this approximation for getting B_z or B_x from J_y for that voxel (at an observation point outside the figure). A line current I_y is positted running from the center of one face straight across the element to the opposite face. The current is J_y integrated across the face, i.e. $J_y l_x l_z$, and is dependent on E_y, the electric field, which is easily calculated:

$$E_y = ((\phi_5 + \phi_6 + \phi_7 + \phi_8) - (\phi_1 + \phi_2 + \phi_3 + \phi_4))/4l_y \tag{2.25}$$

For a corner that is shared by the full complement of 8 voxels, B_x receives a negative contribution for the 4 voxels behind in the y-axis, and a positive one for the 4 ahead, as shown in equation 2.26, where we let $g(x, y, z)$ stand for the terms of equation 2.28 that depend on the cartesian coordinates:

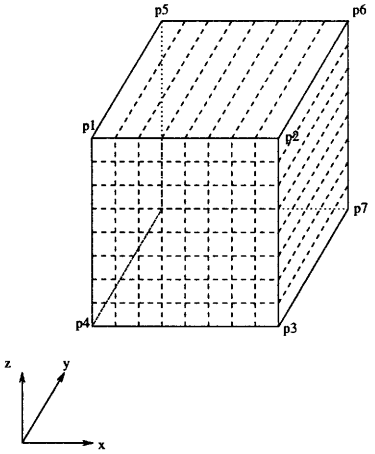

Figure 2-4: Dividing the voxel to obtain an analytical integration of the Biôt-Savart Law.

$$B_x(\phi_1) = \frac{\sigma\mu_0 l_x l_z}{l_y 16\pi}\left(\sum_{behind} g(x,y,z) - \sum_{ahead} g(x,y,z)\right) \tag{2.26}$$

For an isotropic element, J_y is governed by Ohm's Law as below (otherwise it gets contributions from E_x and E_z), and for the potential difference between each opposing pair of points ($\phi_5 - \phi_1$ and so on), for that voxel, B_x gets this contribution:

$$J_y = E_y \sigma l_z l_x \tag{2.27}$$

$$B_x(\phi_5 - \phi_1) = \frac{\mu_0(\phi_5 - \phi_1)\sigma l_x l_z}{l_y 16\pi}\frac{z}{z^2 + x^2}\left(\frac{y + l_y}{\sqrt{x^2 + (y + l_y)^2 + z^2}} - \frac{y}{\sqrt{x^2 + y^2 + z^2}}\right) \tag{2.28}$$

Of course, each pair gives a similar contribution to the field for the other elements it borders. Now to correct for the errors made by approximating the magnetic field as a line segment, we can split the two faces in a grid, and calculate for the line segments made by Figure 2.3, summing up as need be. As the subdivisions reach infinitessimal size, equation 2.23 becomes this:

$$B_x = \frac{\mu_0 J_y}{4\pi}\iint \frac{z}{z^2 + x^2}\left(\frac{y + l_y}{\sqrt{x^2 + (y + l_y)^2 + z^2}} - \frac{y}{\sqrt{x^2 + y^2 + z^2}}\right)dx\,dz \tag{2.29}$$

The integral above can be separated to two terms that integrate in the x and z axes the same way, here's one term:

$$B_x = \frac{\mu_0 J_y}{4\pi} \iint \frac{z}{z^2+x^2} \frac{y}{\sqrt{x^2+y^2+z^2}} dx\, dz \tag{2.30}$$

It first integrates into the following:

$$B_x = \frac{\mu_0 J_y}{4\pi} \int \tanh^{-1} \frac{\sqrt{x^2+y^2+z^2}}{y} dx \tag{2.31}$$

And then, integrating along the z axis, we get

$$\begin{aligned} B_x = \frac{\mu_0 J_y}{4\pi} \Big(& - x \tanh^{-1} \frac{\sqrt{x^2+y^2+z^2}}{y} \\ & - y \log \left(x + \sqrt{x^2+y^2+z^2}\right) \\ & - z \tan^{-1} \left(\frac{z}{x}\right) \\ & - z \tan^{-1} \left(\frac{xz}{y\sqrt{x^2+y^2+z^2}+y^2+z^2}\right)\Big) \end{aligned} \tag{2.32}$$

The inverse arctangent function gives a complex number for arguments larger than unity. The imaginary part is cancelled, however, by the summation we make for the 8 invocations of this expression per voxel. (The imaginary part is always $\pi/2$.) The real part of the inverse arctangent is equal to

$$\Re(\tanh^{-1} \alpha) = \frac{1}{4} \log \frac{(\alpha+1)^2}{(\alpha-1)^2}. \tag{2.33}$$

Entering into equation 2.32 we get:

$$\begin{aligned} B_x = \frac{\mu_0 J_y}{4\pi} \Big(& - \frac{x}{4} \log \left(\frac{(\sqrt{x^2+y^2+z^2}+y)^2}{(\sqrt{x^2+y^2+z^2}-y)^2}\right) \\ & - y \log \left(x + \sqrt{x^2+y^2+z^2}\right) \\ & + z \tan^{-1} \left(\frac{z}{x}\right) \\ & - z \tan^{-1} \left(\frac{xz}{y\sqrt{x^2+y^2+z^2}+y^2+z^2}\right)\Big) \end{aligned} \tag{2.34}$$

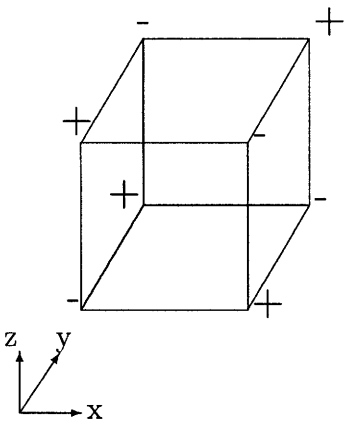

Figure 2-5: Summing the definite integral over the 8 vertices.

This is the end result of integrating the Biôt Savart Law over three dimensions. To turn this into a definite integral the formula is calculated for the 8 vertices of the hexahedral element, and added as shown by figure 2.3. This sum is then added to the source terms for points 5 through 8, and subtracted from the source terms for points 1 through 4. It is important to note that a node that is within the volume will have 4 positive and 4 negative contributions from the 8 voxels around it. Its source term will therfore not be as strong as that of a node on the boundary of the volume, whose terms will not be partly balanced this way, though it will be stronger if the voxels surrounding it differ sharply in conductivity.

The next step is to take into account that under the linear hexahedral element model, the current density in the y direction through a voxel may vary in the x, z directions. We should now consider the varying density j_y. Along the line from point 5 to point 1 it takes this form:

$$j_y = \frac{\sigma(\phi_1 - \phi_5)}{l_y} \tag{2.35}$$

From point 1 to 2 it varies linearly to the respective value for the line from 6 to 2:

$$j_y = \frac{\sigma(\phi_1 - \phi_5)}{l_y}\frac{x_2 - x}{l_x} + \frac{\sigma(\phi_2 - \phi_6)}{l_y}\frac{x - x_1}{l_x} \tag{2.36}$$

And the same variation takes place in the z direction:

$$\begin{aligned} j_y = & \frac{\sigma(\phi_1 - \phi_5)}{l_y} \frac{x_2 - x}{l_x} \frac{z - z_4}{l_z} \\ & + \frac{\sigma(\phi_2 - \phi_6)}{l_y} \frac{x - x_1}{l_x} \frac{z - z_3}{l_z} \\ & + \frac{\sigma(\phi_3 - \phi_7)}{l_y} \frac{x - x_4}{l_x} \frac{z_2 - z}{l_z} \\ & + \frac{\sigma(\phi_4 - \phi_8)}{l_y} \frac{x_3 - x}{l_x} \frac{z_1 - z}{l_z} \end{aligned} \tag{2.37}$$

The linear variation through the element, of the current density component of interest, allows us to treat separately the current components decided by each of the four pairs of points. This makes it easier to calculate the source configuration for the reciprocity model. Inserting this definition into equation 2.29 and taking into account only points 5 and 1, we reach this formula for B_x as generated by that edge of the voxel:

$$B_x = \frac{\mu_0 \sigma(\phi_1 - \phi_5)}{4\pi l_x l_y l_z} \iint \frac{(x_2 - x)(z - z_4)z}{z^2 + x^2} \frac{y}{\sqrt{x^2 + y^2 + z^2}} dz\, dx \tag{2.38}$$

At first pass it integrates as follows:

$$\begin{aligned} B_x = \frac{\mu_0 \sigma(\phi_1 - \phi_5)}{4\pi l_x l_y l_z} \int & (x_2 - x) y \log\left(z + \sqrt{x^2 + y^2 + z^2}\right) \\ & + (x_2 - x) x (\tan^{-1} \frac{z}{x} - \tan^{-1} \frac{xz}{x^2 + y^2 + y\sqrt{x^2 + y^2 + z^2}}) \\ & + (x_2 - x) z_4 \tanh^{-1} \frac{\sqrt{x^2 + y^2 + z^2}}{y} dx \end{aligned} \tag{2.39}$$

The second integration provides us with:

$$B_x = -\frac{\mu_0\sigma(\phi_1-\phi_5)}{4\pi l_x l_y l_z}(F_1+F_2+F_3+F_4) \tag{2.40}$$

$$\begin{aligned}
F_1 &= x_2z_4x\tanh^{-1}\frac{\sqrt{x^2+y^2+z^2}}{y} + x_2z_4y\log\left(x+\sqrt{x^2+y^2+z^2}\right) \\
&\quad + x_2z_4z\left(\tan^{-1}\frac{z}{x} + \tan^{-1}\frac{xz}{z^2+y^2+y\sqrt{x^2+y^2+z^2}}\right) \\
F_2 &= \frac{1}{2}z_4\left((x^2+y^2+z^2)\tanh^{-1}\frac{\sqrt{x^2+y^2+z^2}}{y} + y\sqrt{x^2+y^2+z^2} - \frac{y^2}{2}\log\frac{\sqrt{x^2+y^2+z^2}+y}{\sqrt{x^2+y^2+z^2}-y}\right) \\
F_3 &= x_2xy + \frac{x_2(x^2+z^2)}{2}\tan^{-1}\frac{z}{x} - \frac{x_2x^2}{2}\tan^{-1}\frac{xz}{x^2+y^2+y\sqrt{x^2+y^2+z^2}} \\
&\quad + \frac{x_2z^2}{2}\tan^{-1}\frac{xz}{z^2+y^2+y\sqrt{x^2+y^2+z^2}} - x_2y^2\tan^{-1}\frac{x}{y} - \frac{x_2y^2}{2}\tan^{-1}\frac{y}{x} \\
&\quad - \frac{x_2y^2}{2}\tan^{-1}\frac{xy}{z^2+y^2+z\sqrt{x^2+y^2+z^2}} - \frac{x_2xy}{2}\log\left(z+\sqrt{x^2+y^2+z^2}\right) \\
F_4 &= \frac{x^3}{3}\tan^{-1}\frac{xz}{x^2+y^2+y\sqrt{x^2+y^2+z^2}} + \frac{y(x^2+y^2)}{2}\log\left(z+\sqrt{x^2+y^2+z^2}\right) \\
&\quad - \frac{yz\sqrt{x^2+y^2+z^2}}{6} - \frac{y(x^2+y^2+z^2)}{4} - \frac{x^3}{3}\tan^{-1}\frac{z}{x} \\
&\quad - \frac{z^3}{6}\log\frac{\sqrt{x^2+y^2+z^2}+y}{\sqrt{x^2+y^2+z^2}-y} - \frac{y^3}{6}\log\frac{\sqrt{x^2+y^2+z^2}+z}{\sqrt{x^2+y^2+z^2}-z}
\end{aligned}$$

This greatly complicated formula must be summed up for the 8 points that define the element. Since it defines the contributions of points 5 and 1, it is summed up as in figure 2.3 and then added to point 5's source term and subtracted from point 1's. The same paradigm applies for all 6 orientations we might have. To apply these formulae in a different direction, replace x with the dimension of the sensor orientation, y with the dimension of the current components being summed, and z with the dimension that is ignored. To calculate B_x, it is necessary to repeat this procedure for the current components in the z-direction. And to calculate B in an arbitrary direction, we must have a weighted sum of all 6 orientations.

Equation 2.40 accounts for the magnetic field generated by the isotropic case. In an anisotropic element, a potential difference in the x direction will generate a current in the y direction, i.e. $\vec{j_y} = \sigma_{xy}\vec{E_x}$ where σ_{xy} is the xy component of the local

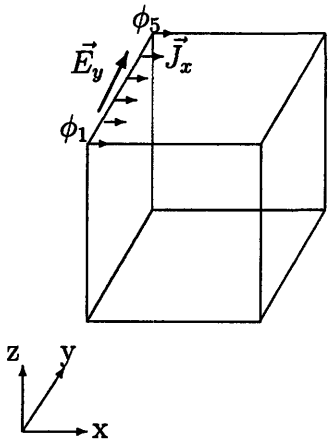

Figure 2-6: The field in the y-direction produces a current in the x-direction.

conductivity tensor. As we move along the line going from point 5 to 1 this current density component stays constant since it is induced by a constant electric field in the y-direction. Moving along the x-direction, this component declines linearly down to zero (to be replaced by the linearly increasing component brought on by points 2 and 6). The same decline applies in the z-direction. Since the current is in the x-direction, it is only of concern if we are calculating B_y or B_z. But if the voxel is anisotropic, then to obtain B_x we must the current components in the z and y directions, and these receive contributions from all three Cartesian directions. To demonstrate one case of this, let's look at the y-current induced by the electric field in the x-direction. This current density is in the y-direction but it stays uniform in the x-direction and varies in the y and z directions. If the edge of interest is that between points 1 and 2 then equation 2.38 requires backtracking to the triple integral (equation 2.14) and inserting the details of our coordinate system to produce the following integral and its counterpart for y-currents induced by the electric field in the z-direction:

$$B_x = \frac{\mu_0 \sigma_{xy}(\phi_1 - \phi_2)}{4\pi l_y^2 l_z} \iiint \frac{(z - z_4)(y - y_5)yz}{(x^2 + y^2 + z^2)^{3/2}} dy\, dx\, dz \tag{2.41}$$

$$B_x = \frac{\mu_0 \sigma_{xz}(\phi_1 - \phi_4)}{4\pi l_y l_x l_z} \iiint \frac{(x - x_2)(y - y_5)yz}{(x^2 + y^2 + z^2)^{3/2}} dy\, dx\, dz \tag{2.42}$$

This integral must be put in closed form, evaluated over the 8 vertices, and then added to point 2's source term and subtracted from point 1's. And so, by putting

together all the field components that generate the current components that a sensor will observe, and making it the source distribution for our Poisson's equation solver we get a lead-field with which we can build a fast forward solver for the magnetoencephalogram.

2.4 Summary

The finite difference reciprocity model for MEG works as follows: first, we assemble a finite difference mesh that reflects the conductivity distribution of the volume in question. Here it is the model published by Saleheen[28]. Then, for each pair of nodes in the mesh, we calculate the contribution they would make to the magnetic field at the given sensor location and orientation, per volt of potential difference between them. We add that coefficient to the mesh's source term for each and every node.

$$b_{node} = \frac{1}{l_x l_y l_z} \frac{\mu_0}{4\pi} \sum_{elements} \iiint \frac{\sigma \vec{\nabla} \psi \times \hat{R}}{R^2} dv \Big|_{vertices} \quad (2.43)$$

In principle the method is shown above. Each node's source term is the sum, for each of the elements that it borders, of the contribution the element makes to the magnetic field. Rather than integrating the Biôt Savart Law for the currents in the volume, we integrate it for the basis function of each node. In this thesis the integral is put in the approximate form shown by Equation 2.34. The finite difference solver is then run to find the potential distribution induced by this fictitious source distribution. Then, for any current dipole in the model, one finds the magnetic field induced by the dipole by taking the dot product of the dipole moment $\vec{Q}$ and the gradient of the fictitious potential ϕ and adding the field generated by the primary current.

$$\vec{B} = \vec{B_0} + \vec{Q} \cdot \vec{\nabla} \phi \quad (2.44)$$

$$\vec{B_0} = \frac{\mu_0 \vec{Q} \times \vec{r}}{4\pi} \quad (2.45)$$

Chapter 3

Computational Implementation

3.1 Successive Over Relaxation

The successive over-relaxation method is an obvious choice for this sparse formulation because it is fast and has the smallest memory footprint of the common iterative equation solvers in the literature [27, 12]. It is fast and easy to write up from scratch, although its performance in the literature is not the best compared to several other methods[21]. It is represented below for any matrix equation $Ax = b$, with n equations and unknowns :

for i = 1 to n

$$x_i^{(k+1)} = \omega(b_i - \sum_{j=1}^{i-1} a_{ij}x_j^{(k+1)} - \sum_{j=i+1}^{n} a_{ij}x_j^{(k)})/a_{ii} + (1-\omega)x_i^{(k)} \quad (3.1)$$

end

The algorithm begins with a guess to the solution $x^{(k)}$ and improves it iteratively through the algorithm above. ω is the over-relaxation parameter that is adjusted for faster convergence and depends on the eigenvalues of A. When it is set to 1, the iteration is equivalent to the Gauss-Seidell iteration. Each step in this method only modifies one member of the solution vector. For sparse cases like ours each member only looks at a few neighbors when it is modified.

In order to make the fastest use of this method we should look at a related one, the Jacobi iteration, presented here:

$$\begin{aligned} &\text{for i = 1 to n} \\ &\quad x_i^{(k+1)} = (b_i - \textstyle\sum_{j=1}^{i-1} a_{ij} x_j^{(k)} - \sum_{j=i+1}^{n} a_{ij} x_j^{(k)})/a_{ii} \\ &\text{end} \end{aligned} \tag{3.2}$$

The key difference is that when SOR builds the next solution vector $x^{(k+1)}$ out of the previous $x^{(k)}$, at each step it looks at members of both $x^{(k+1)}$ and $x^{(k)}$, while the Jacobi method only looks at the $x^{(k)}$ solution vector, as it was at the start of the iteration. SOR coverges to a solution faster than the Jacobi iteration, and is in fact more numerically stable.

To see why, visualize the Jacobi iteration beginning with an all-zero $x^{(0)}$ for a volume containing a current dipole. Our volume has three dimensions, X, Y, and Z, and its nodes are indexed from 1 to n such that $i = x + X(y-1) + XY(z-1)$, such that x, y, z in the expression are the Cartesian coördinates of each node. At first, only those members that coincide on the dipole location, those x_i such that $b_i \neq 0$, are made non-zero. At the next iteration the neighboring members are filled in, and then their neighbors, and so on. For a cubic volume sized 100^3, it would take at least 50 iterations and possibly as many as 99 before all members are nonzero. In contrast, SOR, having reached the dipole location, begins to fill in every value $x_i^{(k)}$ whose index i is higher than those of the dipole.

With this in mind an advantage emerges for the symmetric SOR method, which [21], oddly enough, did not examine. By running up the list of nodes, and then down, we speed up the convergence of this method. A further intuitive step comes from looking at how we map each node in the finite difference representation into its index in the matrix, which is by selecting the fastest and slowest changing dimensions and sweeping up all three as we sweep up from 1 to n. In order to make SOR converge the fastest, we can take the algorithm above for a single row of voxels, sweep up, then

go to the next row, sweep down, again to the next row, sweep up, then down, and so on and so forth for each slice of the volume. Carrying out SOR in this fashion also means having fewer processor cache hits and thus provides an additional speedup. Mathematically it is equivalent to performing SOR on a permutation of the matrix A.

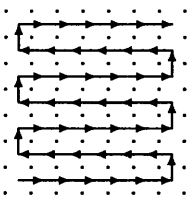

Figure 3-1: The boustrophedon updating order for SOR

3.2 Parallel Implementation

The SSOR iteration is easily parallelized in a one dimensional partitioning scheme, as shown by Figure 3.2, using the Message Passing Interface. The problem is spread to several processes, each of which applies the iteration to a section of the forward matrix, and then communicates with one or two neighbors, giving them the potential distribution for points they need for their own purposes. Each process has a set of points at the edges (represented by the shaded areas), which after calculating it must send up or down (represented by the curved arrows). The size of the point set sent each way between neighbors is effectively that of one slice in our context.

For a partitioning into N processes, the ideal speeding up of the solution is itself a factor of N. By Amdahl's Law, however, we know that the processes will be slowed down by the need to communicate with their neighbors [1]. So long as the number of processes doesn't approach that of slices in the dataset, the partitioning will still leave the iteration mostly computation-dependent. We can also use features in the MPI standard to allow communication and computation to occur simultaneously. Also, a process can perform the SSOR iteration on its section multiple times for every

communication phase. Doing so effectively means computing the Poisson equation with a Von Neumann boundary condition at the physical boundaries of the volume conductor and a Dirichlet boundary condition at the communication boundaries. The Dirichlet condition is set by a preliminary solution of the equation by the neighboring processes, and is thus best updated as often as possible, but a 1 for 1 ratio for communication steps and computation steps is not necessary.

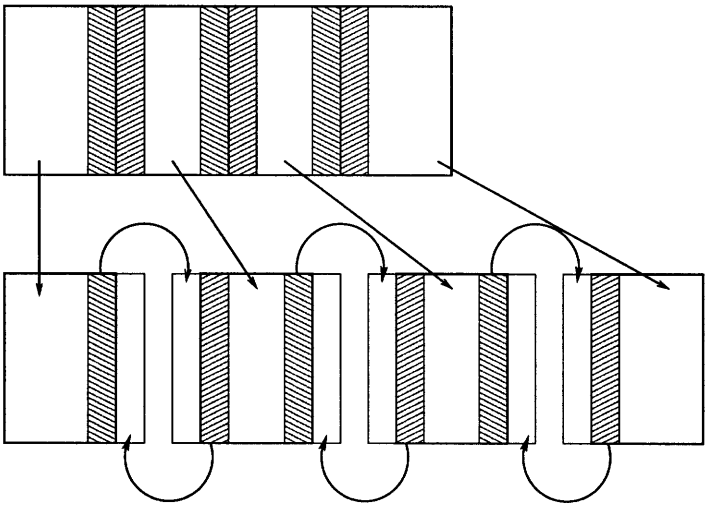

Figure 3-2: The one dimensional partitioning for SSOR

3.3 Convergence

The standard way to represent a dipole source in a finite element mesh is to place a current source on one node and a sink on an adjacent one. The method has drawbacks. It was empirically shown by Schimpf et al[31] not to be well validated against the spherical EEG model. One reason is best explained by the Fourier method of characterizing the discretization error of the finite element method. A dipole source is concentrated in regular space, but its energy is diffuse in three-dimensional Fourier space. The finite element method suffers aliasing error when it is used to represent sources that are diffuse in k-space. Schimpf et al recommend not using adjacent nodes in representing a dipole. The finite difference reciprocity model for the MEG certainly qualifies for that criterion.

Another problem is that using iterative solvers for the forward solution for a dipole is slow. A diffuse source configuration will converge much faster, and this provides another noteworthy advantage to this method. The residual error criterion $||Ax - b||$ is what is most commonly used to measure the convergence of a linear sparse matrix equation. For a volume that is a 120mm diameter sphere, stair-cased into 1mm voxels, the reciprocity forward model takes 7400 iterations of SSOR to bring the residual down 25 orders of magnitude from the starting point. A simple dipole running through this finite difference model would take over 10 times that many iterations to reach the same convergence.

Chapter 4

Validation of the Forward model

4.1 The Multi-layered Concentric Sphere

The first test case for showing the accuracy of the finite-difference-reciprocity solution for the MEG is that of the multilayered sphere, centered at the origin, i.e. $\sigma = f(r)$. An analytical solution for the Biôt Savart integral under spherical symmetry is found in Sarvas et al[30]. Sarvas's formula for the magnetic field is shown below:

$$\vec{B}(\vec{r}) = \frac{\mu_0}{4\pi F^2}(F\vec{Q} \times \vec{r_0} - \vec{Q} \times \vec{r_0} \cdot \vec{r}\vec{\nabla}F) \tag{4.1}$$

Here $\vec{Q}$ is the dipole vector, $\vec{r_0}$ is its location, $\vec{r}$ is the point where the field is observed, and F and $\vec{\nabla}F$ are given below:

$$\begin{aligned} F &= a(ra + r^2 - \vec{r_0} \cdot \vec{r}) \\ \vec{\nabla}F &= (\frac{a^2}{r} + \frac{\vec{a} \cdot \vec{r}}{a} + 2a + 2r)\vec{r} - (a + 2r + \frac{\vec{a} \cdot \vec{r}}{a})\vec{r_0} \\ \vec{a} &= \vec{r} - \vec{r_0}, a = |\vec{a}|, r = |\vec{r}| \end{aligned} \tag{4.2}$$

For a primary current that is a current dipole, the radial component of B_0 becomes

$$B_{0r} = \frac{\mu_0 \vec{Q} \times \vec{a} \cdot \hat{e}}{4\pi |\vec{a}|^3} \tag{4.3}$$

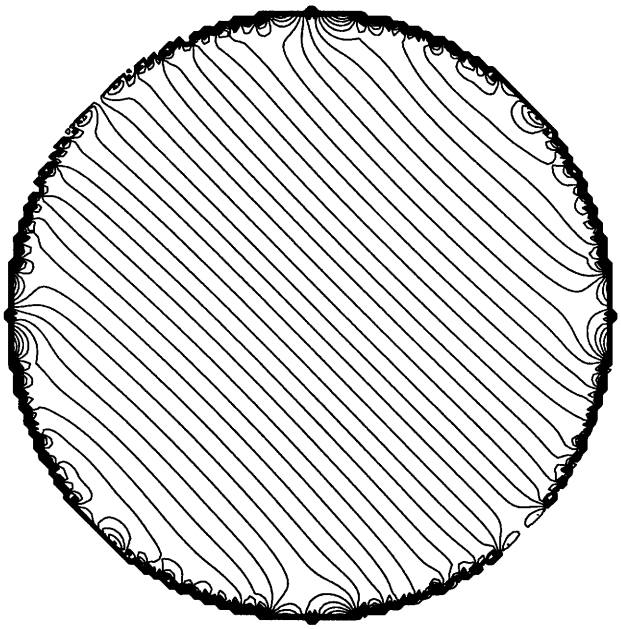

Figure 4-1: Isocontours of the potential in a slice across a spherical test case. Cross section of the x-y plane for a sphere with a sensor placed and oriented on the z-axis.

where $\hat{e}$ points in the radial direction at the location of the dipole.

A current dipole in a sphere, oriented radially, generates no magnetic field outside the sphere at all. Only the tangential component of the dipole will generate a field outside the sphere. A tangentially oriented dipole will generate a magnetic field whose radially oriented component will simply equal that of the primary field, with no contribution from the return currents. The tangential component of the field, however does contain a contribution from the return currents.

So, for a sphere centered at the origin, and a sensor placed on and oriented with the z-axis, the reciprocity model should have a solution with a simple gradient: none. The potential should have a flat distribution. The source terms fed into the model should cancel each other out to enough of an extent that the gradients in the volume be minuscule compared to the primary field B_0.

Alas, this has not been the case. A model of a sphere, 120mm in diameter and divided into cubic voxels of 1mm length was used to test the validity of this model. For the radially oriented sensor, the model produces a potential distribution cutting the sphere to two lobes shown in Figure 4.1 in cross section.

The magnitude of the gradient in the cross section is always within an order of magnitude of that of the primary magnetic field, but its direction (normal to the isopotential contours) does not reflect anything but the distribution of those source terms on the edge of the volume that are not cancelled by their neighbors. The trend held for observations of the field at points 1m from the origin down to 70mm from the origin.

For a sensor on the z-axis, oriented in the y-axis, the result is more encouraging. The primary magnetic field for this case can be generated by dipoles in the z or x directions. An x-y cross section of the reciprocity solution should give a gradient in the x-direction that has a magnitude equal to the difference netween the Sarvas equation's value for the field, minus the primary field. For the test sphere, and for sensors 1m down to 30 mm from the sphere, the gradients hold to between 50% to 200% of the value predicted, for 90% of cross slices through the volume. For closer sensors the difference between reciprocity solution and the Sarvas solution grows.

4.2 Discussion

The magnetic field is not solenoidal: it has a curl, and therefore cannot be described only by a scalar potential. Splitting the field into the components formed by the primary and return currents allows us to try the reciprocity method because only the primary current is non-solenoidal. The return current is defined by scalar electric potential, and can therefore be reformulated in a form that employs reciprocity. Nevertheless, the composition of the source terms is a process that depends on cancellations happening properly. If this method were applied to a cylinder-shaped finite element mesh, with a sensor placed and aligned with the centeral axis, most of the source terms would be daisy-chained and cancelled out. For the same to apply to a Cartesian grid, we must employ a fully closed-form integration of the Biôt Savart law to avoid the systemic errors seen here. Ignoring the source terms on the edges of the model may also reduce this source of systemic error. To gauge the validity of the model would then require testing it against other finite element models and against

real MEG data since the criteria used for such a modification should not be merely the need to match against the spherical model.

The regular finite element method for MEG does not suffer from the errors seen here and can tolerate even cruder approximations of the Biôt Savart law. It is slower, however, because it must be repeated for every dipole, and not just every sensor. Therefore, further development of the finite difference reciprocity model for the MEG remains warranted.

Bibliography

[1] Gene Amdahl. Validity of the single processor approach to achieving large-scale computing capabilities. In *Proceedings of AFIPS Conference*, volume 30, pages 483–485, Reston, VA, 1967.

[2] C. J. Collie. Magnetic fields and potentials of linearly varying current or magnetisation in a plane bounded region. In *Conference on the Computation of Magnetic Fields*, pages 86–95. Rutherford Laboratory, 1976.

[3] Leonid Zhukov David M. Weinstein and C. Johnson. Lead-field bases for electroencephalography source imaging. *Annals of Biomedical Engineering*, 28(9):1059–1065, September 2000.

[4] Jan C. de Munck. The potential distribution in a layered anisotropic spheroidal volume conductor. *Journal of Applied Physics*, 64(2):464–470, July 1988.

[5] Jan C. de Munck and Maria Peters. A fast method to compute the potential in the multisphere model. *IEEE Transactions on Biomedical Engineering*, 40(11):1166–1174, November 1998.

[6] Jan C. de Munck, Bob W. Van Dijk, and Henk Sperkreijse. Mathematical dipoles are adequate to describe realistic generators of human brain activity. *IEEE Transactions On Biomedical Engineering*, 35(11):960–966, November 1988.

[7] Peter Fenwick. The inverse problem: a medical perspective. *Physics in Medicine and Biology*, 32(1):5–9, 1987.

[8] A. Stewart Ferguson and Gerhard Stroink. Factors affecting the accuracy of the boundary element method in the forward problem – i: calculating the surface potentials. *IEEE Transactions on Biomedical engineering*, 44(11):1139–1155, 1997. http://ieeexplore.ieee.org/xpl/tocresult.jsp?isNumber=13893.

[9] S. Finke and R. M. Gulrajani. Conventional and reciprocal approaches to the forward problem of electroencephalography. *Electromagnetics*, 21(7-8):513–530, 2001.

[10] S. Finke and R. M. Gulrajani. Conventional and reciprocal approaches to the inverse dipole localization problem of electroencephalography. *IEEE Transactions on Biomedical Engineering*, 2003.

[11] Thomas Frodl, Georg Juckel, Jürgen Gallinat, Ronald Bottlender, Markus Riedel, Ulrich Preuss, Hans-Jürgen Möller, and Ulrich Hegerl. Dipole localization of p300 and normal aging. *Brain Topography*, 13(1):3–8, 2000.

[12] Gene H. Golub and Charles F. Van Loan. *Matrix Computations*, pages 510–512. Johns Hopkins, Baltimore, Maryland, USA, 3 edition, 1996.

[13] Matti Hämäläinen, Riitta Hari, Risto J. Ilmoniemi, Jukka Knuutila, and Olli V. Lounasmaa. Magnetoencephalography–theory, instrumentation, and applications to noninvasive studies of the working human brain. *Review of Modern Physics*, 65(2):413–497, April 1993.

[14] Jens Haueisen, Ceon Ramon, Michael Eiselt, Hartmut Brauer, and Hannes Nowak. Influence of tissue resistivities on neuromagnetic fields and electric potentials studied with a finite element model of the head. *IEEE Transactions on Biomedical Engineering*, 44(8):727–735, August 1997.

[15] Jens Haueisen, David S. Tuch, Paul H. Schimpf, V. J. Wedeen, J. S. George, and J. W. Belliveau. The influence of brain tissue anisotropy on human EEG and MEG. *NeuroImage*, 15:159–166, 2002.

[16] M. Huang, Cheryl J. Aine, Selma Supek, Elaine Best, Douglas Ranken, and E.R. Flynn. Multi-start downhill simplex downhill simplex method for spatio-temporal source localization in magnetoencephalography. *Electroencephalography and clinical neurophysiology*, 108:32–44, 1998.

[17] A. A. Ioannides, J.P.R. Bolton, and C.J.S. Clarke. Continuous probabilistic solutions to the biomagnetic inverse problem. *Inverse Problems*, 6:523–542, 1990.

[18] Derek Kenton Jones, Steve Charles Rees Williams, David Gasston, Mark Andrew Horsfield, Andrew Simmons, and Robert Howard. Isotropic resolution diffusion tensor imaging with whole brain acquisition in a clinically acceptable time. *Human Brain Mapping*, 15:216–230, 2002.

[19] Päivi Laarne, Jary Hyttinen, Silke Dodel, Jaakko Malmivuo, and Hanno Eskola. Accuracy of two dipolar inverse algorithms applying reciprocity for forward calculation. *Computers and Biomedical Research*, 33:172–185, 2000.

[20] Jian Le and Alan Gevins. Method to reduce blur distortion from EEG's using a realistic head model. *IEEE Transactions on Biomedical Engineering*, 40(6):517–528, June 1993.

[21] M. Mohr and Bart Vanrumste. Comparing iterative solvers for linear systems associated with the finite difference discretization of the forward problem in electro-encephalographic source analysis. *Medical & Biological Engineering & Computing*, 41(1):75–84, January 2003.

[22] F. Moradi, L.C. Liu, K. Cheng, R.A. Waggoner, K. Tanaka, and A. A. Ioannides. Consistent and precise localization of brain activity in human primary visual cortex by MEG and fMRI. *NeuroImage*, 18:595–609, August 2003.

[23] John C. Mosher and Richard M. Leahy. Recursive music: a framework for EEG and MEG localization. *IEEE Transactions on Biomedical engineering*, 45(11):1342–1354, November 1998.

[24] John C. Mosher, Richard M. Leahy, and Paul S. Lewis. EEG and MEG: forward solutions for inverse methods. *IEEE Transactions on Biomedical engineering*, 46(3):245–259, March 1999.

[25] Roberto Domingo Pascual-Marqui. Review of methods for solving the EEG inverse problem. *International Journal of Bioelectromagnetism*, 1(1):75–86, 1999.

[26] Robert Plonsey. *Engineering Contributions to Biophysical Electrocardiography.* IEEE Press selected reprint series. IEEE Press, New York, 1982.

[27] William H. Press, Saul A. Teukolsky, William T. Vetterling, and Brian P. Flannery. *Numerical Recipes in C.* Cambridge, 2 edition, 1992.

[28] Hasan I. Saleheen and Kwong T. Ng. New finite difference formulations for general inhomogeneous anisotropic bioelectric problems. *IEEE Transactions on Biomedical Engineering*, 44(9):800–809, 1997.

[29] Hasan I. Saleheen and Kwong T. Ng. A new three-dimensional finite-difference bidomain formulation for inhomogeneous anisotropic cardiac tissues. *IEEE Transactions on Biomedical engineering*, 45(1):15–25, January 1998.

[30] Jukka Sarvas. Basic mathematical and electromagnetic concepts of the biomagnetic inverse problem. *Physics in Medicine and Biology*, 32(1):11–22, 1987.

[31] Paul H. Schimpf, Ceon Ramon, and Jens Haueisen. Dipole models for the EEG and MEG. *IEEE Transactions on Biomedical Engineering*, 49(5):409–418, May 2002.

[32] Mingui Sun. An efficient algorithm for computing multishell spherical volume conductor models in EEG dipole source localization. *IEEE Transactions on Biomedical Engineering*, 44(12):1243–1252, December 1997.

[33] S. Thees, F. Blankenburg, B. Taskin, G. Curio, and A. Villringer. Dipole source localization and fMRI of simultaneously recorded data applied to somatosensory organization. *NeuroImage*, 18:707–729, August 2003.

[34] David S. Tuch. *Diffusion MRI of Complex Tissue Structure.* PhD thesis, Massachusetts Institute of Technology, 2002.

[35] Areti Tzelepi, Andreas A. Ioannides, and Vahe Poghosyan. Early (n70m) neuromagnetic signal topography and striate and extrastriate generators following pattern onset quadrant stimulation. *NeuroImage*, 13(4):702–718, April 2001.

[36] R. Van Uitert and C.R. Johnson. Can a spherical model substitute for a realistic head model in forward and inverse meg simulations? August 2002.

[37] R. Van Uitert and C.R. Johnson. Influence of brain conductivity on magnetoencephalographic simulations in realistic head models. page (Accepted), September 2003.

[38] R. Van Uitert, David M. Weinstein, and Christopher R. Johnson. Volume currents in forward and inverse magnetoencephalographic simulations using realistic head models. *Annals of Biomedical Engineering*, 31:21–31, 2003.

[39] R. Van Uitert, David M. Weinstein, C.R. Johnson, and Leonid Zhukov. Finite element EEG and MEG simulations for realistic head models: Quadratic vs. linear approximations. In *3rd International Symposium On Noninvasive Functional Source Imaging*, 2001.

[40] S. P. van den Broek, H. Zhou, and M. J. Peters. Computation of neuromagnetic fields using finite-element method and the biot-savart law. *Medical & Biological Engineering & Computing*, 34(1):21–26, 1996.

[41] B. Vanrumste, G. Van Hoey, P. Boon, M. D'Havé, and I. Lemahieu. Inverse calculations in EEG source analysis applying the finite difference method, reciprocity and lead fields. In *Proceedings of the 20th Annual International Conference of the IEEE Engineering in Medicine and Biology Society* [], pages 2112–2115.

[42] Bart Vanrumste. *EEG dipole source analysis in a realistic head model.* PhD thesis, Universiteit Gent, 2002.

[43] Bart Vanrumste, Gert Van Hoey, Rik Van de Walle, Michel R.P. D'Havé, Ignace A. Lemahieu, and Paul A.J.M. Boon. The validation of the finite difference method and reciprocity for solving the inverse problem in EEG dipole source analysis. *Brain Topography*, 14(2):83–92, Winter 2001.

[44] Blaise Yvert, Anne Crouzeix-Cheylus, and Jacques Pernier. Fast realistic modeling in bioelectromagnetism using lead-field interpolation. *Human Brain Mapping*, 14:48–63, 2001.

[45] Zhi Zhang. A fast method to compute surface potentials generated by dipoles within multilayered anisotropic spheres. *Physics in Medicine and Biology*, 40:335–349, 1995.

[46] H. Zhou. Computation of the potential distribution in a four-layer anisotropic concentric spherical volume conductor. *IEEE Transactions on Biomedical Engineering*, 39:154–158, February 1992.

[47] Leonid Zhukov, David M. Weinstein, and C. R. Johnson. Reciprocity basis for EEG source imaging. *NeuroImage*, 2000.